HyperMSM: a New MSM Variant for Efficient Simulation of Dynamic Soft-Tissue Deformations

Abbass Ballit, Tien-Tuan Dao

▶ To cite this version:

Abbass Ballit, Tien-Tuan Dao. HyperMSM: a New MSM Variant for Efficient Simulation of Dynamic Soft-Tissue Deformations. Computer Methods and Programs in Biomedicine, 2022, pp.106659. ⟨10.1016/j.cmpb.2022.106659⟩. ⟨hal-03543510⟩

HAL Id: hal-03543510

https://hal.science/hal-03543510v1

Submitted on 22 Jul 2024

HyperMSM: a New MSM Variant for Efficient Simulation of Dynamic Soft-Tissue Deformations

Abbass Ballit[1], Tien-Tuan Dao[1]

abbass.ballit@centralelille.fr, tien-tuan.dao@centralelille.fr

[1]Univ. Lille, CNRS, Centrale Lille, UMR 9013 LaMcube - Laboratoire de Mécanique, Multiphysique, Multiéchelle, F-59000, Lille, France.

Manuscript submitted as a **Research Paper** to the

Computer Methods and Programs in Biomedicine,

January 11th 2022 (1st Revision)

Corresponding author: Tien Tuan Dao, Ph.D.

Centrale Lille Institut, CNRS UMR 9013 - LaMcube
Laboratoire de Mécanique, Multiphysique, Multiéchelle
59655 Villeneuve d'Ascq Cedex, France
Tel: 33 3 20 43 43 04

E-mail: tien-tuan.dao@centralelille.fr

Abstract

Background and Objective: Fast, accurate, and stable simulation of soft tissue deformation is a challenging task. Mass-Spring Model (MSM) is one of the popular methods used for this purpose for its simple implementation and potential to provide fast dynamic simulations. However, accurately simulating a non-linear material within the mass-spring framework is still challenging. The objective of the present study is to develop and evaluate a new efficient hyperelastic mass-spring model formulation to simulate the Neo-Hookean deformable material, called HyperMSM.
Methods: Our novel HyperMSM formulation is applicable for both tetrahedral and hexahedral mesh configurations and is compatible with the original projective dynamics solver. In particular, the proposed MSM variant includes springs with variable rest-lengths and a volume conservation constraint. Two applications (transtibial residual limb and the skeletal muscle) were conducted.
Results: Compared to finite element simulations, obtained results show RMSE ranges of [2.8%-5.2%] and [0.46%-5.4%] for stress-strain and volumetric responses respectively for strains ranging from -50% to +100%. The displacement error range in our transtibial residual limb simulation is around [0.01mm-0.7mm]. The RMSE range of relative nodal displacements for the skeletal psoas muscle model is [0.4%-1.7%].
Conclusions: Our novel HyperMSM formulation allows hyperelastic behavior of soft tissues to be described accurately and efficiently within the mass-spring framework. As perspectives, our formulation will be enhanced with electric behavior toward a multi-physical soft tissue mass-spring modeling framework. Then, the coupling with an augmented reality environment will be performed.

Keywords: *hyperelastic material, mass-spring model, Neo-Hookean solid, soft tissue deformation, real-time simulation.*

I. INTRODUCTION

The dynamic simulation of soft tissue deformation has attracted many researchers in the last few decades [1]. It shows potential interests in educational applications toward an enhanced property-function relationship learning and in clinical routine practices (i.e. diagnosis, surgical planning) of musculoskeletal disorders. In particular, the surgical simulation requires both realistic and real-time modeling of soft tissue responses to tool-tissue interactions [2],[3]. To achieve such a complex system, three constraints related to computation speed, simulation stability, and system accuracy should be satisfied. However, these constraints are closely dependent since performance improvement of one aspect is mainly achieved by the detriment of the other one. Computation speed is defined as the number of computing iterations that a soft-tissue simulator can execute in one second using a specific hardware configuration. On the other hand, system accuracy is defined as the accuracy of the results of the simulated soft-tissue deformations with respect to the in vivo biological tissue physiology. Soft tissues are known to have hyper-visco-elastic properties. They exhibit anisotropic, heterogeneous, and nearly incompressible behaviors [4]. Soft tissues have been commonly modeled using a passive material in surgical simulation applications while active behaviors of soft tissues are still challenging due to complex model formulation and model accuracy [5]. In particular, the most frequently used material models are Neo-Hookean, Mooney-Rivlin, Yeoh, and Ogden formulations [6] implemented with the Finite Element Method (FEM). This approach is based on a continuum formulation of the governing behaviors of soft tissues. Despite a very good accuracy level, FEM in its conventional formulations is well-known for its expensive computation time and simplified assumptions (i.e. small deformation and dis-placements) making it not suitable for real-time interactive applications with large deformations and rotations such as surgical simulators. Some variants of the FEM such as precomputation-based FEM or formulation-adapted FEM have been also proposed [2]. However, the computational time and complex stress-strain formulation are still challenging for a real-time medical simulation system.

In addition to the FEM, other computational methods and models have been developed to simulate soft tissue deformations in real-time [2], [7]. Early methods used geometrically-based approaches, such as free-form deformation (FFD) [8] and deformable splines [9]. These approaches are fast for interactive soft-tissue deformations, but they do not provide realistic results. Other deformable models such as extended Position-Based Dynamics (xPBD) [10], [11], or shape-matching technique [12] have been also used for fast soft tissue deformations. However, PDB and shape-matching approaches are mainly based on geometrical constraints instead of real physical properties. In particular, the shape-matching technique relies on the determination of an optimal cluster stiffness coefficient for realistic soft-tissue deformations, without considering the physical properties of soft tissues. One of the widely used approaches for modeling soft tissue deformations [13] is the Mass-Spring Model (MSM), also known as Mass-Spring System (MSS). This approach has been implemented in several surgical simulation applications such as gall bladder surgery [9], virtual severed blood vessel microsurgery [14], subject-specific pelvic system surgery [15], heart valves [16], transurethral resection of prostate [17], and endoscopic surgery [18]. The choice of this approach is often motivated by its simple constitutive equation formulation and its potential capacity to perform real-time computations with satisfactory physical accuracy. However, the determination of accurate and reliable spring parameters (e.g. stiffness and damping factors) and optimal topological configurations remains a challenging issue. Several variant approaches have been proposed to enhance the volume preservation mechanism using specific constraints [19] or penalty forces [20]. The latter approach has been followed by Baudet et al. [21] with additional forces in terms of the Poisson ratio. In addition, Golec et al. [22] formulated these forces from the volume variation energy and proposed the MSS-CF (Mass-Spring System - Corrective Forces) model. In our previous study, we proposed also a new variant of MSM with corrective springs and variable stiffness, called MSS-CS (Mass-Spring System with corrective springs) model [23]. Moreover, to scope with the nonlinear materials, Teschner et al. [24] used non-linear stiffness formulation as a function of deformation with multi-layered spring configuration. This approach has been followed later by other work [25]. Moreover, San-Vicente et al. [13] estimated the stiffness coefficients of the springs from a tensile test of a cubical MSM to model the Ogden hyper-elastic material behavior. Goulette and Chen [26] presented a Hyper-Elastic Mass-Links (HEML) model for fast computation of soft tissue deformation. This model is derived from the FEM formulation with local nodal displacements. Accurately simulating a nonlinear material within the mass-spring framework is still challenging, and even very recent soft tissue modeling methods are still relying on classical MSM derived from the properties of linear elasticity [27]. Despite many efforts done in the literature, the characterization of spring properties needs an explicit formulation as well as enhanced mechanical tests for parameter identification and calibration.

A few years ago, Projective Dynamics (PD) [28] has been proposed as a robust, stable, fast, and accurate method to solve the time integration of a mechanical dynamic simulation. It is based on the projection of a given constraint to the manifold containing all the possible solutions of this constraint at its zero level. This method is however limited to some models whose constitutive laws can be reformulated in a PD style. Later, this method has been interpreted as a particular case of a Quasi-Newton Method [29] or even an Alternating Direction Method of Multipliers (ADMM) [30]. These methods provide generalized formulations that support more material models such as hyperelastic ones which were not supported by the original PD. Projective Dynamics is an attractive method, and it can link to a model reduction approach [31] providing a much faster simulation that is independent of the mesh resolution of the model. This fact is desirable for interactive applications requiring real-time interaction with high-resolution meshes. Kugelstadt et al. (2018) [32] proposed a fast corotated finite element method using operator splitting. The results show extreme speed-up compared to other methods. However, this method is presented to be compatible with the linear corotated models and the possibility to apply it to hyperelastic materials has not been investigated. Xie et al. (2021) [33] applied the explicit integration scheme known for its high calculation speed, combined with extended Kalman filter to eliminate the model overshooting and overcome the instability of the explicit method.

Whereas many constitutive laws have been developed especially for soft tissues (either polynomial or exponential models), they all stay equivalent to the neo-Hookean within certain deformation range [34]. Neo-Hookean model is simple and relatively efficient in term of computation. This fact makes it an efficient simplification of the soft tissue deformations and has been widely used for this purpose [35–39]. In the present study, we present a new model, compatible with the PD formulation, to simulate a hyperelastic material, the Neo-Hookean in particular. This model is based on a mass-spring system whose springs have variable rest-length to match the hyperelastic behavior, coupled with a volume preservation constraint. We will call this model “HyperMSM” which stands for “Hyper-elastic Mass-Spring Model”. This approach combines the robustness, rapidity, and stability of the PD with the simplicity, ease of implementation, and low computational cost of the mass-spring system. The next section of this paper will discuss the methodology of the present study including the theoretical background and model formulations, the identification of the model’s parameters, the implementation, and the validation experiments. The experimental results are then shown in the “Results” section, followed by a “Discussions” section to discuss the outcomes, the contributions, and the limitations. Finally, the “Conclusions” section provides a summary of the study and perspectives.

II. METHODS

II.1. Neo-Hookean Constitutive Law

The Neo-Hookean solid is a hyperelastic material that is usually defined by its strain energy density function as follows:

$$\widehat{W}_{Neo-Hookean} = C_{10}(\bar{I}_1 - 3) + \frac{1}{D_1}(J-1)^2 \tag{1}$$

where I_1 and I_2 are the two invariants of the left Cauchy-Green deformation tensor as follows:

$$I_1 = \lambda_1^2 + \lambda_2^2 + \lambda_3^2 \tag{2}$$

where λ_1, λ_2 and λ_3 are the stretch ratios along the three axes, $\bar{I}_1 = J^{-2/3} I_1$, and $J = \lambda_1 \lambda_2 \lambda_3$ represents the volume ratio of the deformable element. C_{10} are the material constants related to the distortional responses whereas D_1 is the incompressibility constants related to the volumetric response. The first term in (1) represents the distortional energy density function, whereas the second term represents the volumetric energy density function.

The constitutive relationships between Neo-Hookean model parameters with linear elastic properties for small deformations are expressed as follows:

$$\begin{cases} C_{10} = \frac{1}{2}\,\mu \\ \frac{1}{D_1} = \frac{1}{2}\kappa \end{cases} \quad with \quad \begin{cases} \mu = \dfrac{E}{2(1+\nu)} \\ \kappa = \dfrac{E}{3(1-2\nu)} \end{cases} \tag{3}$$

where E is the Young modulus, ν is the Poisson ratio, μ is the shear modulus, κ is the bulk modulus.

II.2. Projective Dynamics

Considering a dynamic simulation of a deformable object with a time-step h, and current nodes positions q^t and velocities v^t, the new positions of the model’s nodes q^{t+h} correspond to the critical points of the following function:

$$\begin{aligned} g^t(q^{t+h}) = {} & \frac{1}{2}\,(q^{t+h} - y^t)^T M (q^{t+h} - y^t) \\ & + h^2\left(E(q^{t+h}) - {q^{t+h}}^T F\right) \end{aligned} \tag{4}$$

where M is the diagonal mass matrix, F is the external forces vector, $y^t = q^t + hv^t$ is the predicted position vector if we only consider the pure inertia motion of the system without any forces. $E(q^{t+h}) = \sum_i E_i(q_i^{t+h})$ represents the sum of the deformation-related constraints $E_i(q_i)$ applied to a set of nodes q_i. These constraints are interpreted as the internal energy stored due to the deformation. The formula of such a constraint is usually non-linear which leads to an optimization problem of a non-linear system as follows:

$$q^{t+h} = \underset{q}{\operatorname{argmin}}\, g^t(q) \tag{5}$$

In the projective dynamics, each constraint is to be defined as:

$$E_i^t(q_i^{t+h}) = \frac{\eta_i}{2} \left\| G_i q_i^{t+h} - p_i^t \right\|^2 \tag{6}$$

where η_i is the stiffness of the constraint, G_i is a discrete differential operator represented usually by a sparse matrix, and p_i^t is an auxiliary variable vector representing the projection of the current state to the manifold of all the solutions of $E_i^t(q_i) = 0$. Then, the solver consists of alternating between finding the local projections of each constraint to its manifold (local step) and finding the nodes' positions (global step) by solving $\nabla g^t(q) = 0$ which consists of a system of linear equations with a constant main matrix that does not change during the simulation as long as the mesh connectivity, model parameters, and simulation time-step are constant.

II.3. Mass-Spring System

The potential energy stored in a mass-spring system is defined as follows:

$$E_{springs}(q) = \frac{1}{2}\, q^T L q - \, q^T Q d \tag{7}$$

The internal elastic forces of the springs are given as:

$$F_{springs}(q) = \, -\nabla E_{springs}(q) = -Lq + Qd \tag{8}$$

where L is a Laplacian matrix dependent upon the stiffnesses and the connectivities between the nodes, and Q is a matrix that describes how the nodes are assigned to the springs. The formulas of these matrices are described in [40]. d is a stacked vector representing the steady-state of each spring by a vector whose norm is equal to the rest length and direction is updated following the nodal positions q. In fact, d is non-linear in terms of q, and Projective Dynamics solves this by considering d as the projection of the current state of the springs into their constraints manifolds and therefore updates it in the local step according to the current iterate of q. The locally calculated d is then used in the global step where a system of linear equations is to be solved.

II.4. HYPERMSM

II.4.1. SPRINGS WITH VARIABLE REST LENGTHS

Classical springs exhibit a linear relationship between the applied mechanical load and their response, and they are not able to mimic the hyperplastic behavior no matter how we choose their stiffness constants. In addition, the classical mass-spring model is unable to provide a volume preservation property no matter how the model parameters are chosen. It is very easy to give supportive examples and even prove this analytically. One possible variant of the mass-spring model to handle these limitations is to propose a non-linear stiffness formulation for each spring. However, this approach is not supported by the PD solver. Hereupon, we propose to introduce the concept of the *variable rest lengths* for the springs. For a given spring s, we note k_s the stifness constant, $L_{s,0}^t$ the current value of the variable rest length, and $L_{s,0}$ the initial geometrical length. Thes key point is to vary $L_{s,0}^t$ in terms of the current geometrical length L_s^t so we can get a certain behavior that differs from the linear one. The constitutive equation of the L_0^t is expressed as follows:

$$\begin{cases} L_{s,0}^t = \; L_{s,0} \times (1 + \alpha_1 |\delta_s^t|) \\ \delta_s^t = \dfrac{L_s^t - \, L_{s,0}}{L_{s,0}} \end{cases} \tag{9}$$

where α_1 is a constant that will be determined in Section 3.3.3, and δ_s^t is the deformation ratio of the spring. The absolute value of δ_s^t is used in (9) so $L_{s,0}^t$ is always greater than $L_{s,0}$ with α being positive. Thus, the spring gets stiffer when it is compressed ($L_s^t < L_{s,0}$) and become less stiff when it is stretched ($L_s^t > L_{s,0}$). It is important to note that α_1 should be always less than 1 so that $L_{s,0}^t$ is always less than L_s^t. Otherwise, $L_{s,0}^t$ becomes greater than L_s^t leading to unstoppable elongation. Hence, the condition $0 \leq \alpha_1 < 1$ is to be satisfied.

According to the classical Hook's law, the norm of the internal force of the deformed spring is given as:

$$F_s = k_s\left(L_s^t - L_{s,0}^t\right) \tag{10}$$

If we substitute $L_{s,0}^t$ by its expression given in (9), we can rewrite (10) in the following form:

$$F_s = k_s(1 - sign(\delta_s^t).\alpha_1)\big(L_s^t - L_{s,0}\big) \tag{11}$$

The potential energy stored by the spring can be calculated by integrating (11) in terms of L_s^t, which yields:

$$E_s^t = \frac{1}{2}k_s(1 - sign(\delta_s^t).\alpha_1)\big(L_s^t - L_{s,0}\big)^2 \tag{12}$$

In the PD solver, these springs will be treated similarly to the classical springs following the equation (8). The only difference is within the local step where the rest lengths involved in the calculation of the local projection d should be calculated according to (9). The rest of the process remains the same.

II.4.2. Volume Conservation

To satisfy the volume conservation mechanism, we assign, to each element e of the mesh, the following volumetric constraint:

$$E_e^t = \frac{1}{2}\kappa_e \frac{\big(V_e^t - V_{e,0}\big)^2}{V_{e,0}} \tag{13}$$

where κ_e is the bulk modulus. V_e^t and $V_{e,0}$ are the current and the initial volume of the element respectively. We will note q_e^{t+h} (a $3m_e$-d vector) the stacked vector containing the positions of the element nodes at the new time-step, m_e is the number of element nodes, and p_e^t (a $3m_e$-d vector) is the related auxiliary variable vector as in (6). In our case, the projection to the constraint manifold consists of an element whose volume is equal to the initial volume $V_{e,0}$ and nodes position vector satisfies the following minimization problem:

$$\begin{aligned} &\underset{q_e}{\text{minimize}} \quad \|q_e^{t+h} - q_e\| \\ &\text{Subj. to} \quad V_e(q_e) = V_{e,0} \end{aligned} \tag{14}$$

The volume variation is at its fastest rate when the position vector varies following the direction of $\nabla_q\, V_e(q)$. Hence, we assume that the shortest way to get to an element whose volume is $V_{e,0}$ starting from the current position q_e^t is by following the path given as follows:

$$q_e = q_e^t + \beta_e^t.\nabla\, V_e(q_e^t) \tag{15}$$

Where $\beta_e^t \in \mathbb{R}$ is a parameter to be determined. This assumption is true for small volume variations. Otherwise, this estimation still considers a null volume variation energy (which will always provide a volume conservation behavior) but the found solution is not guaranteed to be the projection of the current state to the constraint manifold. With q_e^t and $\nabla\, V_e(q_e^t)$ are constants within a simulation step, the minimization problem in (14) is thus transformed to the following form:

$$V_e(\beta_e^t) = V_{e,0} \tag{16}$$

Equation (16) is a third-order polynomial equation that provides up to three real solutions. We pick for β_e^t the solution having the smaller absolute value and an opposite sign of the one of $\big(V_e^t - V_{e,0}\big)$ to avoid possible flip of the element.

Taking into consideration that the element is also translating in the space, we consider a stacked vector representing the element center in terms of q_e, $c_e = \frac{1}{m_e}(A_e \otimes I_{3\times3}).q_e$, A_e is an $m_e \times m_e$ constant matrix whose entities are all equal to one. And we express the position vector of the projection element nodes as follows:

$$\begin{aligned} q_e^{*t} &= c_e^{t+h} + (q_e^t - c_e^t) + \beta_e^t.\nabla\, V_e(q_e^t) \\ &= \frac{1}{m_e}(A_e \otimes I_{3\times3}).q_e^{t+h} + p_e^t \end{aligned} \tag{17}$$

With $I_{3\times3}$ is the identity 3×3 matrix and p_e^t=$(q_e^t - c_e^t) + \beta_e^t.\nabla\, V_e(q_e^t)$ is the auxiliary variable vector. The difference between (15) and (17) is that the spatial translation of the center is taken into consideration in the latter one. Therefore, the volumetric constraint can be now expressed in a PD style according to (6) as follows:

$$\begin{aligned} E_e^t &= \frac{\eta_e}{2}\|q_e^{t+h} - q_e^{*t}\|^2 \\ &= \frac{\eta_e}{2}\left\|[I_{m_e \times m_e} - \frac{1}{m_e}(A_e \otimes I_{3\times3})]q_e^{t+h} - p_e^t\right\|^2 \end{aligned} \tag{18}$$

η_e is the constraint stiffness, and it will be determined in the next section.

II.4.3. Parameters Identification

A. The Classical MSM Parameters

The masses of the nodes are calculated using the conventional approach considering the equal distribution of the element mass to the element's nodes.

The spring stiffness is usually expressed in terms of the spring length and the Young modulus assigned to the model. We adopted the formulations given by Van Gelder et al. [41] and Golec [22] for the tetrahedral and hexahedral mesh configurations respectively.

B. Stiffness of the Volumetric Constraint

We substitute the volume variable V_e^t in (13) by its first-order linear approximation $V_{e,0} + \nabla V_e^{T} . \Delta q$ which yields the following energy formula:

$$E_e^t = \frac{\kappa_e}{2} \frac{\left\|\nabla V_e^{T} . \Delta q_e^{t+h}\right\|^2}{V_{e,0}} \tag{19}$$

The term Δq_e^{t+h} is the difference between the nodal positions vector to be calculated and the nodal position vector related to the projection to the energy manifold. The two vectors ∇V_e^{T} and Δq_e^{t+h} have the same direction according to (19), and therefore, equation (15) can be reformulated as follows:

$$E_e^t = \frac{\kappa_e}{2V_{e,0}} \left\|\nabla V_e^{T}\right\|^2 . \|q_e^{t+h} - q_e^{*t}\|^2 \tag{20}$$

The stiffness of the constraint expressed in (18) is therefore:

$$\eta_e = \frac{\kappa_e}{V_{e,0}} \|\nabla V_e\|^2 \tag{21}$$

∇V_e is variable during the deformation and therefore η_e is variable. We choose to use a linear regression approximation for η_e:

$$\eta_e = \alpha_2 \frac{\kappa_e}{V_{e,0}} \left\|\nabla V_{e,0}\right\|^2 \tag{22}$$

where α_2 is constant to be identified (see Section 3.3.3), and $\nabla V_{e,0}$ is the gradient of the volume at the rest state. For instance, for a regular cubical element whose dimension is a, $\left\|\nabla V_{e,0}\right\|^2 = \frac{3}{2}a^4$, whereas in the case of a regular tetrahedral element, $\left\|\nabla V_{e,0}\right\|^2 = \frac{1}{12}a^4$.

C. The Model Constants

The used approach to identify the values of the constants α_1 and α_2 is based on an optimization approach minimizing the error between the potential energy of our model and the energy of the Neo-Hookean material. We used a dataset of (λ_j, J_j) points generated by combination of set of λ values ranging from 0.5 to 2.0 with a set of J values ranging from $\Gamma(0.5)$ to $\Gamma(2.0)$, where $J = \Gamma(\lambda)$ represents the analytical relationship between λ and J for a Neo-Hookean material under uniaxial stress.10 sample values are extracted for each variable, and therefore the size of the entire (λ_j, J_j) dataset is equal to 100. For each point of this dataset, we calculated the related energies stored by a HyperMSM and a Neo-Hookean element model respectively. The former energy is noted W_j^H and combines both the springs energies expressed in (12) and the volumetric energy expressed in (18), and the latter one is noted W_j^N and it is calculated by multiplying the energy density function given in (1) by the element's volume. Finally, we defined an objective minimizing function consisting of the weighted mean-squared-error of our model's calculated energies with respect to Neo-Hookean ones as follows:

$$\emptyset(\alpha_1, \alpha_2) = \frac{1}{N} \sum_{j=1}^{N} [\omega_i(W_j^H(\lambda_j, J_j, \alpha_1, \alpha_2) - W_i^N(\lambda_j, J_j))]^2 \tag{23}$$

where ω_j is the weight assigned to each dataset point and it is equal to $W_j^N(J, \lambda) / \sum W_j^N(J, \lambda)$. $\emptyset(\alpha_1, \alpha_2)$ is a quadratic function in terms of both α_1 and α_2 and therefore minimizing it is straightforward. This optimization problem tries to fit the analytical Neo-Hookean energy densities with the energy densities of our model. It depends on material properties (Neo-Hookean constants and their equivalent linear elasticity constants) but it is independent of the size of the model. The function in (23) considers the energy densities, the stretching ratios and the volumetric ratios which are all normalized with respect to the size. Results for several Poisson ratios are shown in Table 1.

TABLE 1
Results of the Optimization Problem

ν	α_1	α_2	WRMSE
0.40	0.654	2.18	0.0517
0.425	0.663	1.90	0.0502
0.45	0.672	1.75	0.0464
0.475	0.695	1.62	0.0464
0.49	0.699	1.44	0.0398

ν is the Poisson ratio and WRMSE stands for Weighted Root-Mean-Squared-Error which is the square root of the function Φ.

II.4.4. Implementation

Our simulation environment was developed by using C++ programming language. We used OpenGL for 3D rendering and the Eigen library (eigen.tuxfamily.org) for the linear algebra while solving the minimization problem of (4) according to (5). Since we are using the Projective Dynamics as time integration solver, the time-step h should be constant throughout the simulation. The user interface provides the possibility to tune this parameter to set the simulation speed. Note that a real time simulation is achieved when h is equal to the average real calculation time of each simulation step. In the present implementation, no parallelization of the code has been applied. As for the model damping, we implemented the Laplacian damping proposed in [42] for the projective dynamics solver. All simulations were performed using a Dell Intel® Core™ i7-10850H workstation:

II.4.5. Accuracy & Performance Analysis

A. Accuracy Analysis

The accuracy of our novel HyperMSM formulation with respect to the FE Neo-Hookean model has been analyzed using three types of tests: a uniaxial tensile test (for normal compression behavior analysis), the cantilever bending test (for shear behavior analysis), and twisting test.

The uniaxial tensile test includes both elongation and compression experiments by applying engineering stress to a generic cubical element. It has been performed with two different Young modulus values (100KPa and 1MPa) and three different Poisson ratio values equal to 0.40, 0.45, and 0.49 since the soft tissues are nearly incompressible and they generally have a Poisson ratio close to 0.5 [43], [44].

The bending test was applied to a cantilever model whose dimensions are $0.04\times0.04\times0.1$ m^3 subject to a -9.8m/s^2 gravity. The material properties of the model were set up as follows: 100KPa Young modulus, 1060Kg/m^3 density [45], with the three different Poisson ratio values (0.40, 0.45, and 0.49). Several mesh resolutions wer used for both tetrahedral and hexahedral configurations.

The same cantilever model was used in the twisting test. We applied different three different moment values (0.1Nm, 0.2Nm, and 0.3Nm) to the free extremity surface of the cantilever and we measured the rotating angle at the rest state.

Note that the FE simulations were performed using Abaqus whose outcomes were taken as reference for our results. The default linear elements were used for the hexahedral meshes, whereas both linear and quadratic elements were used in the case of tetrahedral FE models

B. Performance Analysis

The calculation speed of our model was measured by reporting the time required to calculate one time-step for different model resolutions. We compared these measurements with the ones performed using the classical mass-spring model without the additional volume preservation constraint and rest-length calculations.

As for the stability and robustness of the simulation, it is known that these properties are dependent upon the applied time integration method. We used the projective dynamic method with very stable simulations in the present work. Our only concern was if the new formulation of the variable rest-length, expressed in (12), would affect the stability since it is not a differentiable function at the zero point. However, we did not notice this happening during our experiments. Anyway, we show a simulation of a complex deformable geometry recovered from extreme initial conditions as proof of stability. For this simulation, we used a preborn baby model obtained from FEMONUM project (http://femonum.telecom-paristech.fr/) [46]. The related MSM model has been constructed based on a tetrahedral configuration (Fig. 2a). It consists of 33594 tetrahedral elements and 6877 nodes from which 274 inside the baby body are fixed in the space. The model parameters are set as follows: E = 100KPa and $\nu = 0.40$. The simulation was running using 5 iterations per frame and a time-step equal to 10ms

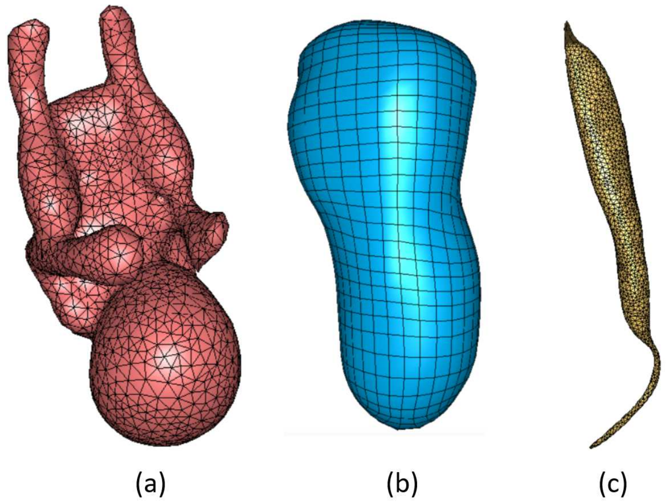

Fig. 2. The biomedical models used in our tests: the preborn model (a), the transtibial residual limb (b), and the right psoas muscle (c)

C. Real-World Applications

To show the robustness and potential applications of our model, two biomechanical models were implemented and simulated using tetrahedral and hexahedral mesh configurations respectively. The first application is a transtibial residual limb reconstructed from CT images for prosthetic socket design. The segmentation and 3D reconstruction process of this model are reported in our previous work [47]. This model (Fig. 2b) consists of 7039 hexahedral elements and 7665 nodes of which 1824 are related to the bony structure and are fixed in the 3D space. We considered for the stump soft tissues a Neo-Hookean model with $C = 11.6KPa$ and $D = 11.9MPa^{-1}$ [48] which is equivalent to a Young modulus $E = 66.538KPa$ and a Poisson ratio $\nu = 0.434$. 10KPa, 30KPa, 50KPa, and 70KPa pressures were applied to the lateral flare of the residual limb.

The second biomechanical model is a right psoas muscle model for muscle stretching simulation under various gravitational forces. The STL geometry of the model was extracted from the Visible Physiological Human project. Then, a tetrahedral volumetric mesh was generated using *Abaqus* (Fig. 2c). The mesh contains 21607 tetrahedral elements and 4769 nodes from which 47 at the extremity of the muscle are fixed in the space. This resolution has been selected following a mesh convergence analysis. We used the muscle material properties proposed by [49] with $C = 66\ KPa$ and $D = 1\ MPa^{-1}$ which is equivalent to a Young modulus $E = 387.476\ KPa$ and a Poisson ratio $\nu = 0.46771$. The model was subject to gravitational force, where different values of gravitational acceleration have been used: 1xg, 10xg, 20xg, and 40xg (g=-9.8m/s^2).

III. RESULTS

III.1. Accuracy Analysis Using Uniaxial Tensile, Bending & Twisting Tests

Fig. 3 shows both normal deflection and volumetric responses during the uniaxial tensile test of the cubical model. The comparison with the analytical Neo-Hookean curves gives a relative root mean square error (RMSE) range of [2.8%-5.2%] for the strain-stress relationship and [0.46%-5.4%] for the strain-volume relationship The higher errors are in fact shown in the case where $\nu = 0.40$, and the model seems to match more the Neo-Hookean material more the Poisson ratio is closer to 0.5. The vertical displacements of the cantilever extremity are given in Fig. 4 and Fig. 5 for the hexahedral and tetrahedral meshes respectively. A good correspondence between the hexahedral HyperMSM model and the FE one is witnessed, with an error equal to 3.7±1.2% for $\nu = 0.40$. This error decreases gradually with higher Poisson ratios and it reaches 8±0.25% for $\nu = 0.45$ and 11.2±0.4% for $\nu = 0.49$. On the other hand, the tetrahedral HyperMSM model behaves more closely to the linear tetrahedral FE model with a relative error equal to 1.6±1.4% for $\nu = 0.40$, 4.4±1.2% for $\nu = 0.45$, and 7.2±0.8% for $\nu = 0.49$, versus 12.7±7.7%, 19.2±8.4%, and 35.6±9.6% respectively compared to the quadratic FE model.

The evolution of the visual deformations of the twisting tests are illustrated in Fig. 6 (a hexahedral case), and Fig. 7 (a tetrahedral case). Generally, a very good qualitative correspondence is witnessed between the results of our model and those coming from the FE simulations. In particular, the outcomes of our tetrahedral model match this time the quadratic FE model. Numerical results are shown in Fig. 8 and Fig. 9 for the hexahedral and the tetrahedral models respectively. We notice that our hexahedral model rotates similarly to the FE model when it is subject 0.1Nm and 0.2Nm moments for both coarse (327 elements) and fine (2500 elements) meshes, an error of 11% of additional rotations is obtained for the fine mesh when it is subject to 0.3Nm moment. Our tetrahedral model behaves similarly but with a dependence of the results upon the mesh resolution. The results of the coarse mesh (420 elements) match the outcomes linear FE model, whereas the fine mesh results (3886 elements) match the quadratic FE ones.

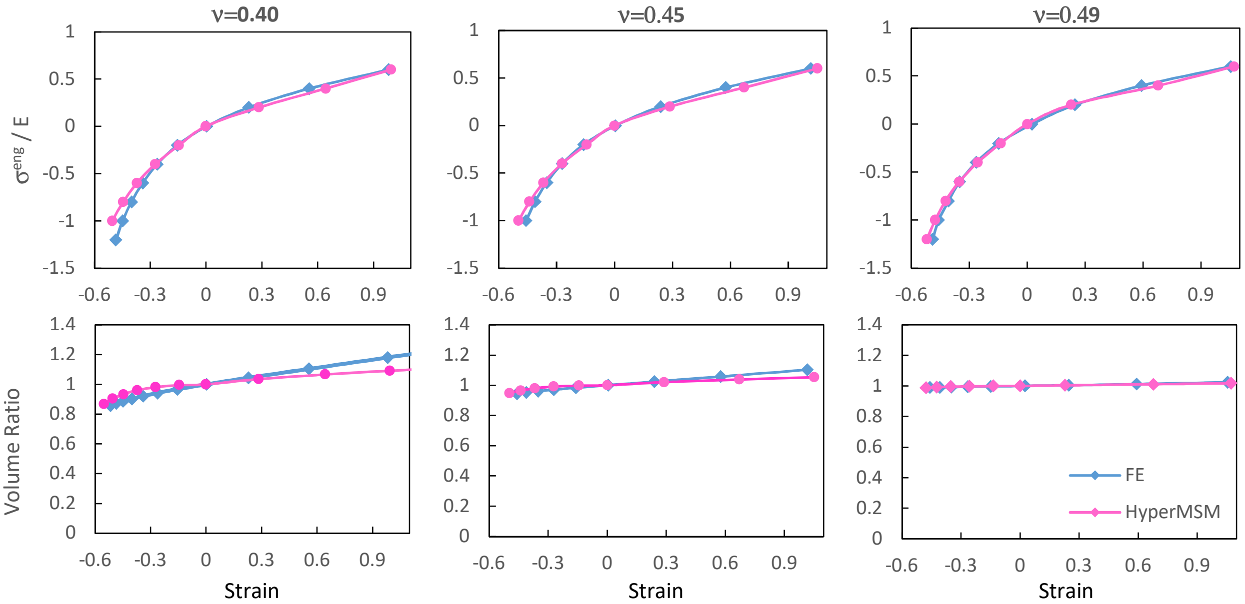

Fig. 3. The results of both normal deflection and volumetric responses of the deformable hexahedral element to a uniaxial tensile test with different values of Poisson ratio ν.

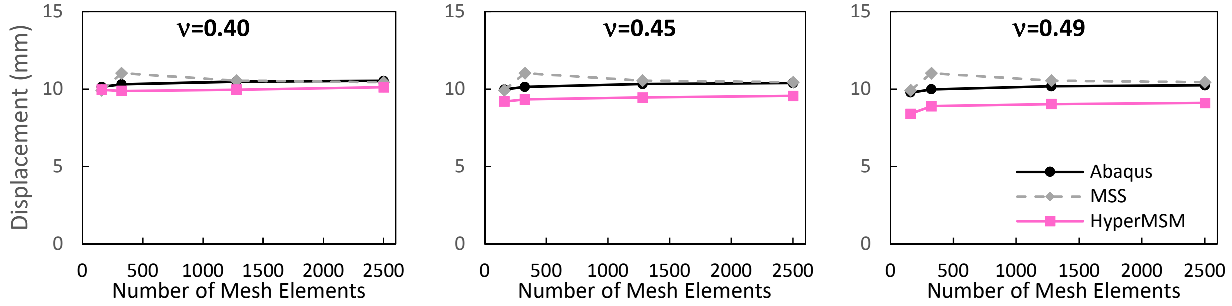

Fig. 4. Vertical displacement of the extremity of the bended cantilever under gravity for different hexahedral mesh resolutions and Poisson ratios ν.

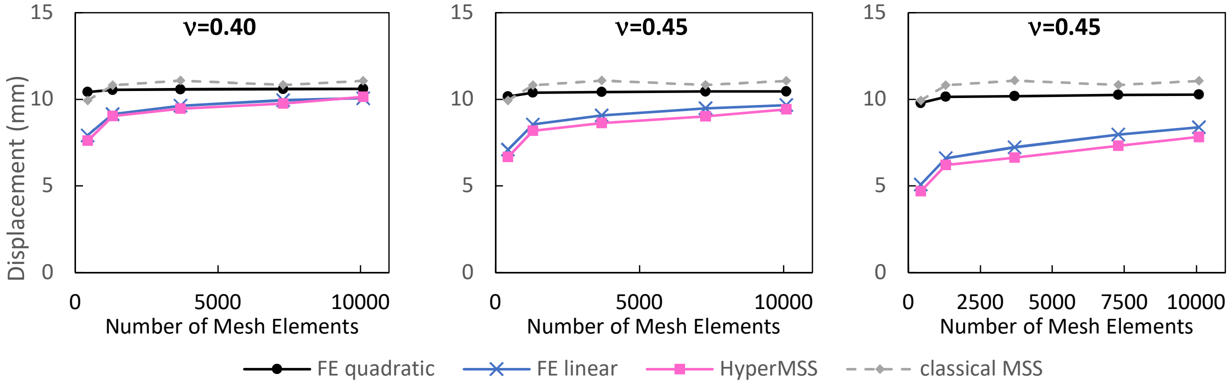

Fig. 5. Vertical displacement of the extremity of the bended cantilever under gravity for different tetrahedral mesh resolutions and Poisson ratios ν.

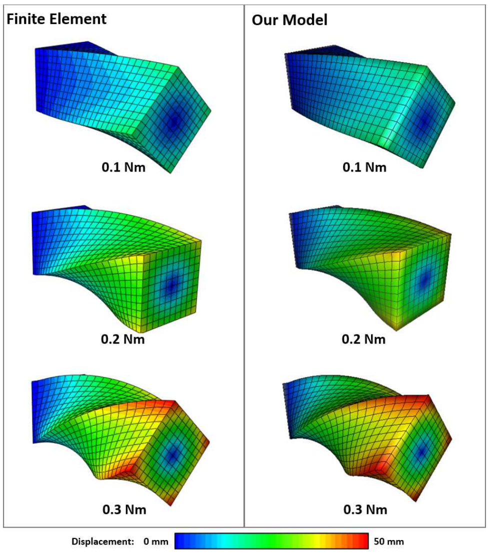

Fig. 6. The visual results of the twisting test applied to a hex-meshed model having 2500 elements and a Poisson ratio ν=0.45.

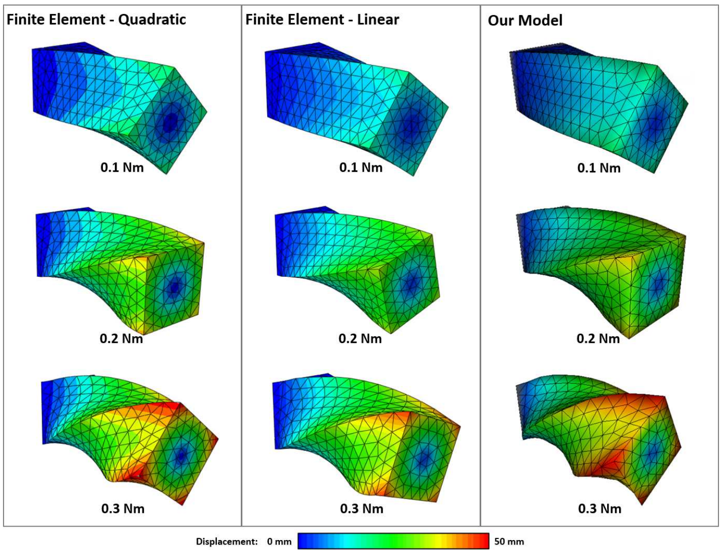

Fig. 7. The visual results of the twisting test applied to a tet-meshed model having 3886 elements and a Poisson ratio ν=0.45.

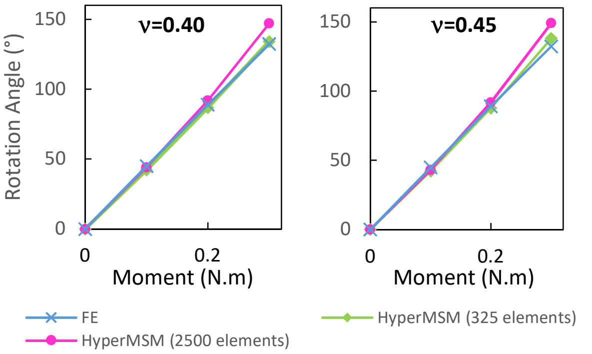

Fig. 8. Evolution of the rotation angle performed by the hex-meshed cantilever beam with respect to the applied moment.

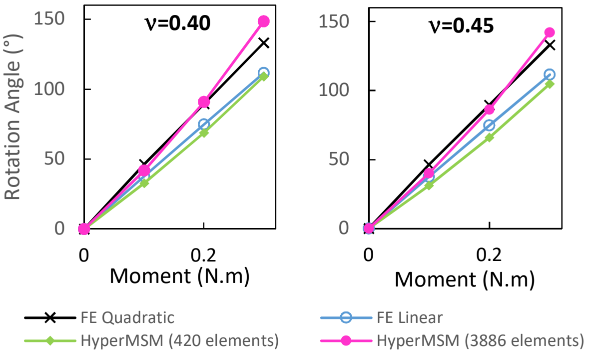

Fig. 9. Evolution of the rotation angle performed by the tet-meshed cantilever beam with respect to the applied moment.

III.2. Performance Analysis: speed and stability

In Fig. 10 we compare the average one-step calculation time between our model and the raw classical MSM model for several mesh settings. We can see that our model is 25% to 50% slower than the classical MSM. We can also notice that the hexahedral model is slower than the tetrahedral model even if the former has a smaller number of elements than the latter. For instance, a 2500-elements hexahedral model requires around 6.9 ms to calculate its simulation step, whereas it is only 3.8 ms for a 10093-elements tetrahedral model. The reason is that, obviously, the hexahedral model holds a larger number of springs than the tetrahedral model: a single hexahedron contains 26 springs, whereas a tetrahedron contains only 6 springs. Consequently, the 2500-elements hexahedral model contains 34 945 springs, and the 10093-elements tetrahedral model contains 13 082 springs.

In Fig. 11 we show six simulation frames of the preborn baby recovery process from an extreme initial condition. (Please refer to the accompanying video for visualizing the full dynamic recovery).

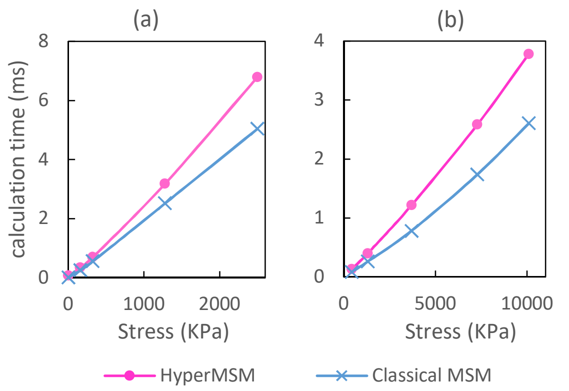

Fig. 10. The computation speed results reported for the hexahedral (a) and tetrahedral (b) bending cantilever models.

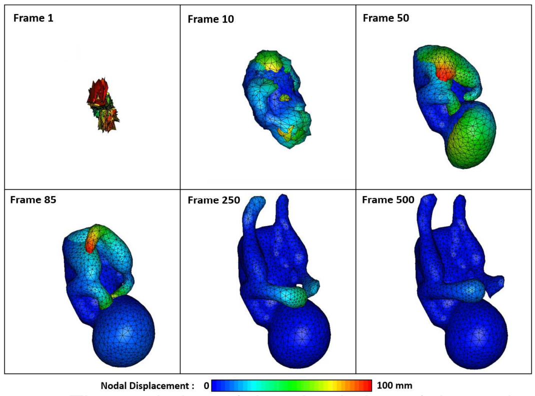

Fig. 11. The evolution of the simulation of the preborn baby recovery process from extreme initial condition.

III.3. Real-world applications: transtibial residual limb

In Fig. 12 we show the visual results of the simulations of the residual limb model under different local normal stresses. Qualitatively, a very satisfying match is witnessed between the FE outcomes and our model ones.

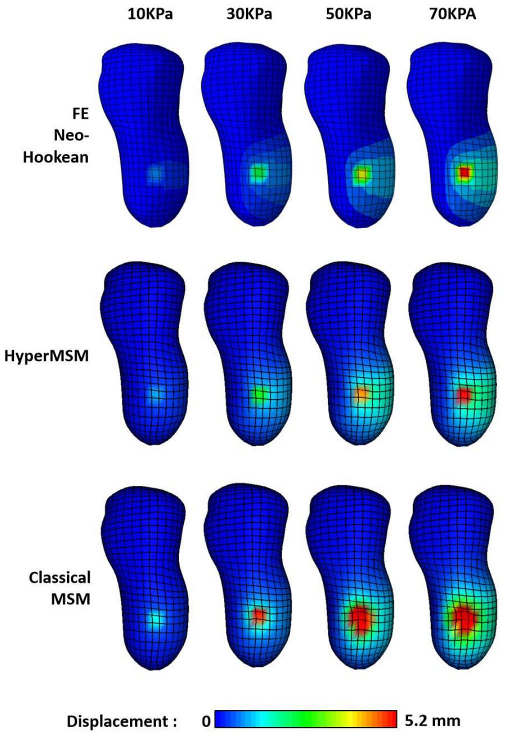

Fig. 12. The visual results of the simulations of the residual limb model subject to a local normal pressure.

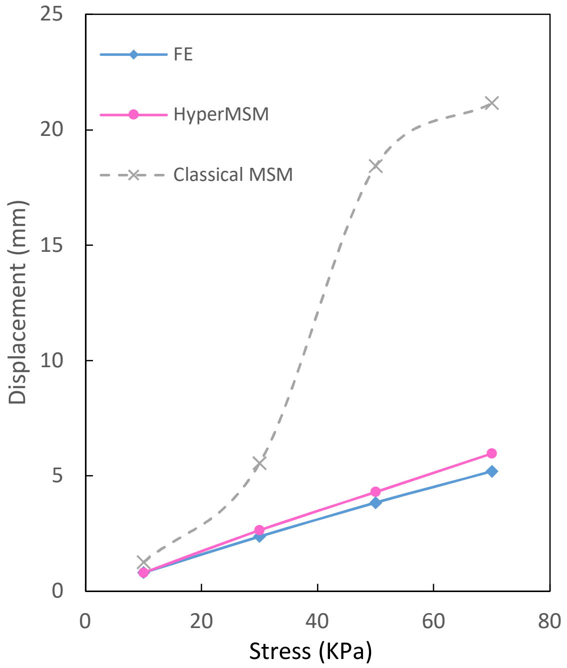

Fig. 13. Comparison of the local displacement values of the stump's surface element subject to normal pressure.

The classical MSM has failed, as expected, to maintain a close displacement range for its elements collapse easily when they are subject to high mechanical loads. A numerical comparison between the normal displacement values resulted from the FE simulation, our HyperMSM model, and the classical MSM is shown in Fig. 13. Our model can follow the FE behavior even with a relatively large mechanical load (a 70KPa pressure value which is larger than the 66.538KPa Young Modulus assigned to the model). The displacement error is equal to [0.01mm-0.7mm].

III.4. Real-World Applications: Right Psoas Muscle

Fig. 14 shows visual displacement evolutions of the models, whereas the numerical results related to the displacement of the free extremity of the muscle for each simulation are given in Fig. 15. A good correspondence to the reference FE results is observed for our model. Precisely, the RMSE range of the overall nodal displacements is [0.4%-1.7%] compared to both linear and quadratic FE outcomes in the case of applied 20g gravity. The errors become higher in the case of larger deformation with applied 40g gravity, where the RMSE values are [1.4%-2.6%] compared to the linear FE model, and [5.2%-6.6%] compared to the quadratic FE mode. The errors observed for the classical MSM are even much higher with a range of [10.9%-14.7%]. Regarding the vertical displacement of the free extremity, the largest errors were witnessed for the higher gravity value (40xg) where HyperMSM gives an error equal to 5.4% with respect to the quadratic FE results and 9.2% with respect to the linear FE. Since this is about an elongation phenomenon, the classical MSM shows the expected higher resistance and therefore lower displacement values, which are overcome by our model thanks to the variable rest-length formulation that provides to the spring a higher dilation capability.

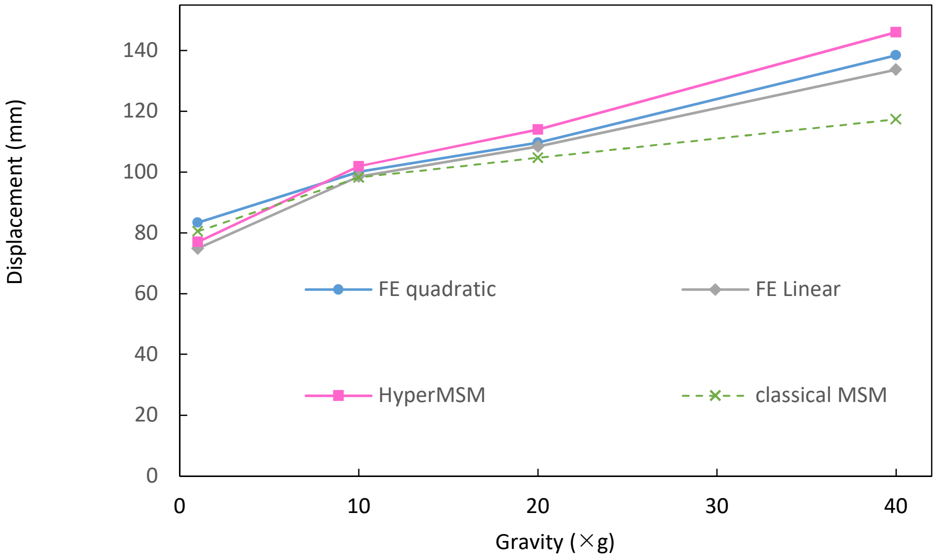

Fig. 15. The maximum displacement values recorded for each simulation of the psoas model.

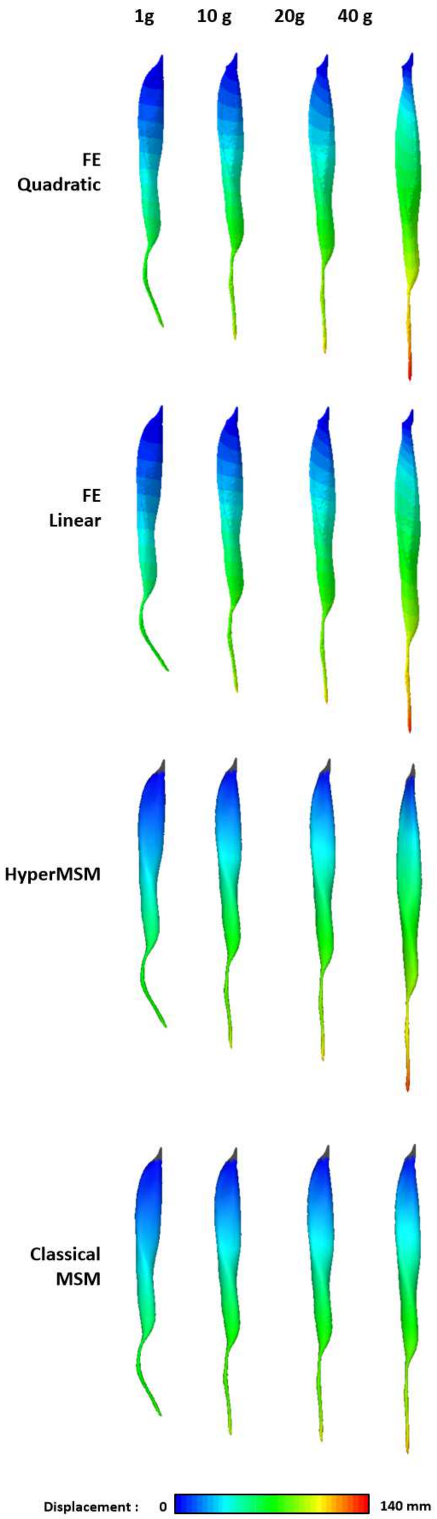

Fig. 14. The visual outcomes of the simulations of the psoas muscle deformation under gravity.

IV. DISCUSSIONS

Soft tissue modeling is a complex engineering task due to its living nature. It has been always a big challenge to simulate soft tissue deformations with both high speed and high accuracy. Previous research studies have investigated multiple engineering approaches ranging from complex finite element methods to mass-spring models (MSM) [5,6,13–23,27]. The discrete MSM is commonly considered as limited due to the avoidance of constitutive equations of the nonlinear elasticity material and volume conservation. Nevertheless, MSM is still an attractive model to simulate real-time deformations for it is characterized by its respectively low computational cost and ease of implementation requiring basic mechanical knowledge. Indeed, masses and springs are very fundamental mechanical elements governed by simple physical laws. Different variants of the MSM approach have been developed to enhance its physical accuracy. One possible improvement relates to the use of formulation derived from continuum formulation [26]. Other solution deals with the FE-informed or experiment-informed identification and calibration for spring parameters (stiffness and damping factor) [13]. Constraint-based strategies have been also investigated for enhancing the volume conservation/preservation constraint with additional corrective forces and springs and energies [22], [23]. Moreover, to obtain more accurate simulation, nonlinear and piecewise linear springs with polynomial spring formulation and deformation-dependent stiffness function have been proposed. Despite many efforts done, a robust formulation of the MSM for soft tissue is still challenging. In this present study, a novel hyperelastic mass-spring model formulation derived from Neo-Hookean formulation, called HyperMSM, was proposed and evaluated. The model introduces variable rest-lengths to the springs for a hyperelastic-like behavior in both compression and elongation cases, and a volume preservation constraint whose parameters are derived from the equivalence formulations between the Neo-Hookean model and the linear elasticity. The constraint has been formulated in PD style so we can apply Projective Dynamics to solve the time integration of the system. Thus, the model inherits the strong points of both MSM (simple and rapid calculations, ease of implementation) and the PD (rapidity, robustness, and high stability even with large simulation time-steps). On the other hand, it is important to note that classical PD does not support hyperelastic materials, and our model has overcome this limitation. Even though PD has been later generalized by a Quasi-Newton method that can support materials satisfying Valanis-Landel assumption (including Neo-Hookean materials), but this costs an additional calculation overhead for an iterative line search performed at each solver iteration [29].

The responses of our HyperMSM model to uniaxial stress and cantilever bending tests are very accurate. The RMSE values are less than 5.2% regarding the uniaxial deflection response and less than 5.4% regarding the volumetric response. The volume change is in good agreement with other study outcomes (<5%) in the literature [13], [19]. Our results are given for strains ranging from -50% to 100% per one mesh element, which is relatively large compared to the results of existing similar works. For instance, Tang et al. (2021) [27] found a good consistency of their results with the reference measurements only for limited deformations. The displacement error range in our transtibial residual limb simulation is around [0.01mm-0.7mm] for our HyperMSM model. Note that San-Vicente et al. (2012) [13] reported a displacement error range of [0.1-1.8] mm for a cubical MSM formulation derived from Ogden formulation. Lloyd et al. (2007) [50] reported a maximal error range of [0.24-1.96] mm and [0.029-1.83] mm for a linear membrane model and an elastic cylindrical solid model respectively. Duan et al. (2016) [19] reported a range of [3.3-4.2] mm for a porcine liver specimen model (26 280 tetrahedral elements).

One important advantage of our novel formulation relates to its applicability to both tetrahedral and hexahedral mesh configurations. Despite the recent progress in the development of hex-meshing tools, it is still not simple to extract a good quality hexahedral mesh from a complex 3D model, and manual interventions are still needed in the process, and it takes forever to be performed [50]. Generally, other approaches focus on the cubical mass-spring models [13], [21], [22], and it is sometimes based on an approximated calculation of the element volume [22]. Our model is applicable with both tetrahedral and hexahedral meshes and considers the exact value of the element volume. This capacity opens new avenues for the application of our proposed variant of the mass-spring model for a large range of applications in the biomedical engineering field, especially in a patient-specific modeling framework. Besides, the tetrahedral models are advantageous over the hexahedral models when it comes to calculation speed, as shown in the results. However, the latter is a more favorable choice when it comes to accuracy. This fact has been already addressed in the literature [17].

The optimization problem expressed in (23) has been applied to a hexahedral element, and the obtained constants (shown in Table 1) were applied to all our simulations even where tetrahedral meshes were used. This is because we found that the results of this optimization problem in the tetrahedral case are not stable, i.e., they are very dependent on how we choose the (λ_j, J_j) dataset. In addition, beside its lower accuracy compared to the hexahedral model, the tetrahedral model sometimes shows undesirable wrinkles with very large deformations that sometimes lead to model collapse. This is a common drawback for the tetrahedral mass-spring models. Fortunately, the volume preservation constraint prevents this to happen most of the time and helps the model to recover in case if it happens.

Our model inherits the advantages as well as the drawbacks of the Projective Dynamics. PD provides a constant approximation of the Hessian matrix of the minimization problem (5). This matrix can be pre-factorized to avoid solving the linear system from scratch at each iteration. However, this requires constant system structure and constant physical parameters. Therefore, PD is not friendly with topological changes (cutting, fracturing) which are commonly required in surgical operations. Li et al (2021) [51] proposed a technique to update the Cholesky factorization of the PD system matrix following localized and gradual topology changes. Another drawback is related to artificial damping. This drawback is generally common for all numerical time integration techniques since they provide an estimation of the exact solution. What is special about PD is the iterative local/global alternation whose formulation considers the translational inertia but does not conserve the rotational one. PD convergence is respectively slow in terms of error evolution with respect to iterations number [28], it can be however accelerated using L-BFGS updates [29]. The selection of the simulation time-step h in (4) plays a big role thereon. Smaller is the time-step, higher is the solution accuracy. However, a real-time simulation often requires a large time-step to be synchronized with the refresh rate, which has an impact to the solver precision and therefore to its convergence. Speed, accuracy, and stability of the simulation are closely dependent parameters since performance improvement of one aspect is mainly achieved by the detriment of the other one [2]. For instance, in the approach of Xie et al. (2021) [33], speed and stability are achieved, but the accuracy at each iterate is questionable since the applied extended Kalman filter eliminates the displacement overshooting based on a statistical model rather than explicit physical model. This implies that a physically exact solution is not always guaranteed, which increases the risk of artificially damping the system for the sake of stability. Our model used the PD solver which always guarantees its convergence to the exact solution per simulation iterate.

Another drawback resides in what we may call “element locking”, caused by the volume preservation constraint, especially when the Poisson ratio approaches the limit of 0.5 making the volumetric forces tend toward infinity. This consists of artificially increased stiffness of the element which prevents it from bending properly, for instance, as shown in our results. This occurs more effectively in the tetrahedral case (Fig. 5). This locking behavior is not witnessed in the case of classical MSM which is free of volumetric preservation constraint, that’s why it shows better bending results than the HyperMSM (Fig. 4 and Fig. 5). A recent study has discussed this issue and proposed a locking-proof tetrahedral model [52]. It is possible to study the applicability of such an approach to our model for higher accuracy. In addition, our model is limited to the Neo-Hookean solids whose equivalent Poisson ratio is greater than 0.4 and does not cover higher-order hyperelastic models such as Mooney-Rivlin or Odgen. Further studies may be carried out to investigate the capabilities of this approach to simulate higher-order polynomial models and various material properties. A higher-order polynomial model of the variable rest-length formulation - instead of the linear model in (9) - may be investigated for this purpose.

V. CONCLUSIONS

A novel mass-spring-based formulation was developed and evaluated to simulate the Neo-Hookean material deformation. This model is also compatible with the robust projective dynamic solver which originally does not support hyperelastic materials. The key contribution relates to the variable rest-length concept for the springs to mimic the hyperelastic behavior in both compression and elongation cases. Our novel HyperMSM formulation allows hyperelastic behavior to be described efficiently and robustly within the MSM framework for both tetrahedral and hexahedral mesh configurations. This opens new avenues for the simulation of large soft tissue deformation in a fast and accurate manner. As perspective, our formulation will be coupled with an augmented reality (AR) environment. We are also looking forward to implementing our model in an AR childbirth training simulator as well as a real-time head animation system for estimating and tracking real-time facial muscle features (e.g. strains and forces) [53].

ACKNOWLEDGMENT

The authors would like to thank the Métropole Européenne de Lille (MEL) and the I-SITE ULNE (Université Lille Nord Europe) for funding.

ETHICAL APPROVAL

This work does not concern any ethical issue.

CONFLICT OF INTEREST

The authors declare that there is no conflict of interest related to the present work.

REFERENCES

[1] C. Basdogan, C.-H. Ho, M.A. Srinivasan, Virtual environments for medical training: graphical and haptic simulation of laparoscopic common bile duct exploration, IEEE/ASME Transactions on Mechatronics. 6 (2001) 269–285. https://doi.org/10.1109/3516.951365.

[2] T.-N. Nguyen, M.-C. Ho Ba Tho, T.-T. Dao, A Systematic Review of Real-Time Medical Simulations with Soft-Tissue Deformation: Computational Approaches, Interaction Devices, System Architectures, and Clinical Validations, Applied Bionics and Biomechanics. 2020 (2020) 1–30. https://doi.org/10.1155/2020/5039329.

[3] H. Delingette, X. Pennec, L. Soler, J. Marescaux, N. Ayache, Computational Models for Image-Guided Robot-Assisted and Simulated Medical Interventions, Proceedings of the IEEE. 94 (2006) 1678–1688. https://doi.org/10.1109/JPROC.2006.880718.

[4] Y.-J. Lim, S. De, Real time simulation of nonlinear tissue response in virtual surgery using the point collocation-based method of finite spheres, Computer Methods in Applied Mechanics and Engineering. 196 (2007) 3011–3024. https://doi.org/10.1016/j.cma.2006.05.015.

[5] T.T. Dao, M.-C.H.B. Tho, A Systematic Review of Continuum Modeling of Skeletal Muscles: Current Trends, Limitations, and Recommendations, Applied Bionics and Biomechanics. 2018 (2018) 1–17. https://doi.org/10.1155/2018/7631818.

[6] R.M. Kenedi, T. Gibson, J.H. Evans, J.C. Barbenel, Tissue mechanics, Physics in Medicine and Biology. 20 (1975) 001. https://doi.org/10.1088/0031-9155/20/5/001.

[7] J. Zhang, Y. Zhong, C. Gu, Deformable Models for Surgical Simulation: A Survey, IEEE Reviews in Biomedical Engineering. 11 (2018) 143–164. https://doi.org/10.1109/RBME.2017.2773521.

[8] T.W. Sederberg, S.R. Parry, Free-form deformation of solid geometric models, ACM SIGGRAPH Computer Graphics. 20 (1986) 151–160. https://doi.org/10.1145/15886.15903.

[9] S.A. Cover, N.F. Ezquerra, J.F. O'Brien, R. Rowe, T. Gadacz, E. Palm, Interactively deformable models for surgery simulation, IEEE Computer Graphics and Applications. 13 (1993) 68–75. https://doi.org/10.1109/38.252559.

[10] J. Pan, J. Bai, X. Zhao, A. Hao, H. Qin, Real-time haptic manipulation and cutting of hybrid soft tissue models by extended position-based dynamics, Computer Animation and Virtual Worlds. 26 (2015) 321–335. https://doi.org/10.1002/cav.1655.

[11] L. Xu, Y. Lu, Q. Liu, Integrating viscoelastic mass spring dampers into position-based dynamics to simulate soft tissue deformation in real time, Royal Society Open Science. 5 (2018) 171587. https://doi.org/10.1098/rsos.171587.

[12] M. Camara, E. Mayer, A. Darzi, P. Pratt, Soft tissue deformation for surgical simulation: a position-based dynamics approach, International Journal of Computer Assisted Radiology and Surgery. 11 (2016) 919–928. https://doi.org/10.1007/s11548-016-1373-8.

[13] G. San-Vicente, I. Aguinaga, J.T. Celigueta, Cubical Mass-Spring Model Design Based on a Tensile Deformation Test and Nonlinear Material Model, IEEE Transactions on Visualization and Computer Graphics. 18 (2012) 228–241. https://doi.org/10.1109/TVCG.2011.32.

[14] J. Brown, S. Sorkin, J.-C. Latombe, K. Montgomery, M. Stephanides, Algorithmic tools for real-time microsurgery simulation, Medical Image Analysis. 6 (2002) 289–300. https://doi.org/10.1016/S1361-8415(02)00086-5.

[15] N. Pirro, M.E. Bellemare, M. Rahim, O. Durieux, I. Sielezneff, B. Sastre, P. Champsaur, Résultats préliminaires et perspectives de la modélisation dynamique pelvienne patient-spécifique, Pelvi-Périnéologie. 4 (2009) 15–21. https://doi.org/10.1007/s11608-009-0231-3.

[16] P.E. Hammer, M.S. Sacks, P.J. del Nido, R.D. Howe, Mass-Spring Model for Simulation of Heart Valve Tissue Mechanical Behavior, Annals of Biomedical Engineering. 39 (2011) 1668–1679. https://doi.org/10.1007/s10439-011-0278-5.

[17] M.A.P. Castañeda, F. Arámbula Cosío, Deformable model of the prostate for TURP surgery simulation, Computers & Graphics. 28 (2004) 767–777. https://doi.org/10.1016/j.cag.2004.06.014.

[18] U. Kühnapfel, H.K. Çakmak, H. Maaß, Endoscopic surgery training using virtual reality and deformable tissue simulation, Computers & Graphics. 24 (2000) 671–682. https://doi.org/10.1016/S0097-8493(00)00070-4.

[19] Y. Duan, W. Huang, H. Chang, W. Chen, J. Zhou, S.K. Teo, Y. Su, C.K. Chui, S. Chang, Volume Preserved Mass–Spring Model with Novel Constraints for Soft Tissue Deformation, IEEE Journal of Biomedical and Health Informatics. 20 (2016) 268–280. https://doi.org/10.1109/JBHI.2014.2370059.

[20] G. Picinbono, H. Delingette, N. Ayache, Non-linear anisotropic elasticity for real-time surgery simulation, Graphical Models. 65 (2003) 305–321. https://doi.org/10.1016/S1524-0703(03)00045-6.

[21] V. Baudet, M. Beuve, F. Jaillet, B. Shariat, F. Zara, Integrating Tensile Parameters in Hexahedral Mass-Spring System for Simulation, in: International Conference on Computer Graphics, Visualization and Computer Vision'2009 - WSCG'2009, hal-00994456, Plzen, Czech Republic, 2009: pp. 145–152.

[22] K. Golec, J.-F. Palierne, F. Zara, S. Nicolle, G. Damiand, Hybrid 3D mass-spring system for simulation of isotropic materials with any Poisson's ratio, The Visual Computer. 36 (2020) 809–825. https://doi.org/10.1007/s00371-019-01663-0.

[23] A. Ballit, I. Mougharbel, H. Ghaziri, T.-T. Dao, Fast Soft Tissue Deformation and Stump-Socket Interaction Toward a Computer-Aided Design System for Lower Limb Prostheses, IRBM. 41 (2020) 276–285. https://doi.org/10.1016/j.irbm.2020.02.003.

[24] M. Teschner, S. Girod, B. Girod, Direct Computation of Nonlinear Soft-Tissue Deformation, in: VMV 2000, Saarbrücken, Germany, 2000.

[25] E. Basafa, F. Farahmand, G. Vossoughi, A non-linear mass-spring model for more realistic and efficient simulation of soft tissues surgery., Studies in Health Technology and Informatics. 132 (2008) 23–5.

[26] F. Goulette, Z.-W. Chen, Fast computation of soft tissue deformations in real-time simulation with Hyper-Elastic Mass Links, Computer Methods in Applied Mechanics and Engineering. 295 (2015) 18–38. https://doi.org/10.1016/j.cma.2015.06.015.

[27] Y. Tang, S. Liu, Y. Deng, Y. Zhang, L. Yin, W. Zheng, An improved method for soft tissue modeling, Biomedical Signal Processing and Control. 65 (2021) 102367. https://doi.org/10.1016/j.bspc.2020.102367.

[28] S. Bouaziz, S. Martin, T. Liu, L. Kavan, M. Pauly, Projective dynamics, ACM Transactions on Graphics. 33 (2014) 1–11. https://doi.org/10.1145/2601097.2601116.

[29] T. Liu, S. Bouaziz, L. Kavan, Quasi-Newton Methods for Real-Time Simulation of Hyperelastic Materials, ACM Transactions on Graphics. 36 (2017) 1–16. https://doi.org/10.1145/2990496.

[30] M. Overby, G.E. Brown, J. Li, R. Narain, ADMM Projective Dynamics: Fast Simulation of Hyperelastic Models with Dynamic Constraints, IEEE Transactions on Visualization and Computer Graphics. 23 (2017) 2222–2234. https://doi.org/10.1109/TVCG.2017.2730875.

[31] C. Brandt, E. Eisemann, K. Hildebrandt, Hyper-reduced projective dynamics, ACM Transactions on Graphics. 37 (2018) 1–13. https://doi.org/10.1145/3197517.3201387.

[32] T. Kugelstadt, D. Koschier, J. Bender, Fast Corotated FEM using Operator Splitting, Computer Graphics Forum. 37 (2018) 149–160. https://doi.org/10.1111/cgf.13520.

[33] H. Xie, J. Song, Y. Zhong, J. Li, C. Gu, K.-S. Choi, Extended Kalman Filter Nonlinear Finite Element Method for Nonlinear Soft Tissue Deformation, Computer Methods and Programs in Biomedicine. 200 (2021) 105828. https://doi.org/10.1016/j.cmpb.2020.105828.

[34] G. Chagnon, M. Rebouah, D. Favier, Hyperelastic Energy Densities for Soft Biological Tissues: A Review, Journal of Elasticity. 120 (2015) 129–160. https://doi.org/10.1007/s10659-014-9508-z.

[35] R. Buttin, F. Zara, B. Shariat, T. Redarce, G. Grangé, Biomechanical simulation of the fetal descent without imposed theoretical trajectory, Computer Methods and Programs in Biomedicine. 111 (2013) 389–401. https://doi.org/10.1016/j.cmpb.2013.04.005.

[36] J. Zhang, R.J. Lay, S.K. Roberts, S. Chauhan, Towards real-time finite-strain anisotropic thermo-visco-elastodynamic analysis of soft tissues for thermal ablative therapy, Computer Methods and Programs in Biomedicine. 198 (2021) 105789. https://doi.org/10.1016/j.cmpb.2020.105789.

[37] C. Chui, E. Kobayashi, X. Chen, T. Hisada, I. Sakuma, Combined compression and elongation experiments and non-linear modelling of liver tissue for surgical simulation, Medical & Biological Engineering & Computing. 42 (2004) 787–798. https://doi.org/10.1007/BF02345212.

[38] B. Ahn, J. Kim, Measurement and characterization of soft tissue behavior with surface deformation and force response under large deformations, Medical Image Analysis. 14 (2010) 138–148. https://doi.org/10.1016/j.media.2009.10.006.

[39] C. Koutras, J. Pérez, K. Kardash, M.A. Otaduy, A study of the sensitivity of biomechanical models of the spine for scoliosis brace design, Computer Methods and Programs in Biomedicine. 207 (2021) 106125. https://doi.org/10.1016/j.cmpb.2021.106125.

[40] T. Liu, A.W. Bargteil, J.F. O'Brien, L. Kavan, Fast simulation of mass-spring systems, ACM Transactions on Graphics. 32 (2013) 1–7. https://doi.org/10.1145/2508363.2508406.

[41] A. van Gelder, Approximate Simulation of Elastic Membranes by Triangulated Spring Meshes, Journal of Graphics Tools. 3 (1998) 21–41. https://doi.org/10.1080/10867651.1998.10487490.

[42] L. Jing, T. Liu, L. Kavan, Laplacian damping for projective dynamics, in: 14th Workshop on Virtual Reality Interactions and Physical Simulations, 2018: pp. 29–36.

[43] Y.-C. Fung, Biomechanics: Mechanical Properties of Living Tissues, illustrated, Springer, 1981.

[44] E.J. Chen, J. Novakofski, W.K. Jenkins, W.D. O'Brien, Young's modulus measurements of soft tissues with application to elasticity imaging, IEEE Transactions on Ultrasonics, Ferroelectrics and Frequency Control. 43 (1996) 191–194. https://doi.org/10.1109/58.484478.

[45] M.G. Urbanchek, E.B. Picken, L.K. Kalliainen, W.M. Kuzon, Specific Force Deficit in Skeletal Muscles of Old Rats Is Partially Explained by the Existence of Denervated Muscle Fibers, The Journals of Gerontology Series A: Biological Sciences and Medical Sciences. 56 (2001) B191–B197. https://doi.org/10.1093/gerona/56.5.B191.

[46] J.P. de la P. Alcalde, J. Anquez, L. Bibin, T. Boubekeur, E. Angelini, I. Bloch, FEMONUM: A Framework for Whole Body Pregnant Woman Modeling from Ante-Natal Imaging Data, in: K. Buehler, A. Vilanova (Eds.), Eurographics 2011 - Dirk Bartz Prize, The Eurographics Association, 2011. https://doi.org/10.2312/EG2011/med/017-020.

[47] A. Ballit, I. Mougharbel, H. Ghaziri, T.-T. Dao, Computer-aided parametric prosthetic socket design based on real-time soft tissue deformation and an inverse approach, The Visual Computer. (2021). https://doi.org/10.1007/s00371-021-02059-9.

[48] S.C. Henao, C. Orozco, J. Ramírez, Influence of Gait Cycle Loads on Stress Distribution at The Residual Limb/Socket Interface of Transfemoral Amputees: A Finite Element Analysis, Scientific Reports. 10 (2020) 4985. https://doi.org/10.1038/s41598-020-61915-1.

[49] R. Lapeer, Z. Gerikhanov, S.-M. Sadulaev, V. Audinis, R. Rowland, K. Crozier, E. Morris, A computer-based simulation of childbirth using the partial Dirichlet–Neumann contact method with total Lagrangian explicit dynamics on the GPU, Biomechanics and Modeling in Mechanobiology. 18 (2019) 681–700. https://doi.org/10.1007/s10237-018-01109-x.
[50] B. Lloyd, G. Szekely, M. Harders, Identification of Spring Parameters for Deformable Object Simulation, IEEE Transactions on Visualization and Computer Graphics. 13 (2007) 1081–1094. https://doi.org/10.1109/TVCG.2007.1055.
[51] J. Li, T. Liu, L. Kavan, B. Chen, Interactive cutting and tearing in projective dynamics with progressive cholesky updates, ACM Transactions on Graphics. 40 (2021) 1–12. https://doi.org/10.1145/3478513.3480505.
[52] M. Frâncu, A. Asgeirsson, K. Erleben, M.J.L. Rønnow, Locking-Proof Tetrahedra, ACM Transactions on Graphics. 40 (2021) 1–17. https://doi.org/10.1145/3444949.
[53] T.-N. Nguyen, S. Dakpe, M.-C. Ho Ba Tho, T.-T. Dao, Kinect-driven Patient-specific Head, Skull, and Muscle Network Modelling for Facial Palsy Patients, Computer Methods and Programs in Biomedicine. 200 (2021) 105846. https://doi.org/10.1016/j.cmpb.2020.105846.

Abbass Ballit received his PhD degree in Biomedical Engineering at the University of Technology of Compiègne (UTC), France in 2020. His current research interests are fast soft tissue deformation, surgical simulations, and computer-aided prosthetic design

Tien-Tuan Dao is Full Professor of Biomedical Engineering and Biomechanics at Centrale Lille Institut, France**.** His research interests concern computational biomechanics, knowledge and system engineering, and *in silico* medicine.